Published online 23 December 2017

Nucleic Acids Research, 2018, Vol. 46, No. 5 ***e30***
doi: 10.1093/nar/gkx1271

(Po)STAC (Polycistronic SunTAg modified CRISPR) enables live-cell and fixed-cell super-resolution imaging of multiple genes

Maria V. Neguembor[1,2], Ruben Sebastian-Perez[1,2], Francesco Aulicino[1,2], Pablo A. Gomez-Garcia[4], Maria P. Cosma[1,2,3,*] and Melike Lakadamyali[4,5,*]

[1]Centre for Genomic Regulation (CRG), The Barcelona Institute of Science and Technology, 08003 Barcelona, Spain, [2]Universitat Pompeu Fabra (UPF), Dr Aiguader 88, 08003 Barcelona, Spain, [3]Institució Catalana de Recerca i Estudis Avançats (ICREA), Pg. Lluís Companys 23, 08010 Barcelona, Spain, [4]ICFO-Institut de Ciencies Fotoniques, The Barcelona Institute of Science and Technology, 08860 Castelldefels (Barcelona), Spain and [5]Perelman School of Medicine, Department of Physiology, University of Pennsylvania, Clinical Research Building, 415 Curie Boulevard, Philadelphia, PA 19104, USA

Received July 26, 2017; Revised November 25, 2017; Editorial Decision December 05, 2017; Accepted December 20, 2017

ABSTRACT

CRISPR/dCas9-based labeling has allowed direct visualization of genomic regions in living cells. However, poor labeling efficiency and signal-to-background ratio have limited its application to visualize genome organization using super-resolution microscopy. We developed (Po)STAC (Polycistronic SunTAg modified CRISPR) by combining CRISPR/dCas9 with SunTag labeling and polycistronic vectors. (Po)STAC enhances both labeling efficiency and fluorescence signal detected from labeled loci enabling live cell imaging as well as super-resolution fixed-cell imaging of multiple genes with high spatiotemporal resolution.

INTRODUCTION

Visualization of endogenous gene loci in living cells is highly valuable for studying dynamic changes to genome organization during any cellular process. Programmable DNA-binding proteins such as clustered regularly interspersed short palindromic repeat (CRISPR)—associated protein 9 (Cas9) have recently been adopted to visualize endogenous repetitive and non-repetitive genomic sequences in living cells (1). This approach relies on the use of a deactivated version of Cas9 lacking enzymatic activity (dCas9) fused to a fluorescent protein (FP), which can be targeted to a number of genomic sequences by using guide RNAs (sgRNAs). The programmable nature of this approach is particularly attractive as it allows targeting a large number of genomic loci. In recent years, this approach has also been adopted to multi-color labeling using orthogonal Cas9 proteins or by introducing RNA aptamers into the sgRNAs (2–5). However, the efficiency of labeling (percentage of cells with fluorescently detectable loci) as well as the amount of fluorescence signal detected from individual loci using this approach have been traditionally low (5,6). The labeling efficiency is limited partially by the efficiency of delivery of many plasmids and partially by the level of expression (5,6). The amount of fluorescence signal detected is limited by the small copy number of dCas9-FPs specifically bound to the locus over a high background introduced by the unbound dCas9-FPs in the nucleoplasm. The low efficiency and low signal combined limit the general applicability of this method for long term, fast imaging of genome dynamics as well as super-resolution imaging of gene architecture. Therefore, a strategy that can boost the detected signal as well as the labeling efficiency is essential.

To overcome these limitations, we took advantage of two separate and complementary strategies: the use of SunTag and polycistronic vectors. SunTag is a repeating peptide array that can be used to recruit multiple copies of an antibody-fusion protein to the target of interest (7). Using this strategy, up to 24 copies of superfolder GFP (sfGFP) fused to the antibody have been recruited to single protein molecules fused to a repeated SunTag array, which is targeted by the antibody. Polycistronic vectors allow the expression of multiple sgRNAs from a single synthetic gene including tRNA–sgRNA modules in tandem. The insertion of the tRNA in between the sgRNAs allows the precise excision of transcripts by the endogenous RNases (8,9). This system has previously been used to demonstrate efficient genome editing in plant and *Drosophila* cells with up to eight sgRNAs (10,11) but has never been validated in mammalian cells and for imaging applications. Here, we fully

*To whom correspondence should be addressed. Tel: +1 215 746 5150; Fax: +1 215 573 2273; Email: melikel@pennmedicine.upenn.edu
Correspondence may also be addressed to Maria Pia Cosma. Tel: +34 93 316 0370; Fax: +34 93 316 00 99; Email: pia.cosma@crg.es

characterized the labeling efficiency of SunTag combined with CRISPR/dCas9, which we termed **STAC** for simplicity (**S**un**TA**g modified **C**RISPR). Further, we developed **PoSTAC** (**Po**lycistronic **S**un**TA**g-modified **C**RISPR) for enhanced genome visualization by combining SunTag alone or SunTag and polycistronic vectors with CRISPR/dCas9.

MATERIALS AND METHODS

Plasmid synthesis

pHRdSV40-dCas9–10xGCN4_v4-P2A-BFP (Addgene # 60903), pHRdSV40-NLS-dCas9–24xGCN4_v4-NLS-P2A-BFP-dWPRE (Addgene # 60910) and pHR-scFv-GCN4-sfGFP-GB1-NLS-dWPRE (Addgene # 60906) were a gift from Ron Vale (7).

pSLQ1658-dCas9-EGFP (Addgene # 51023), pSLQ1651-sgTelomere(F+E) (Addgene # 51024) and pSLQ1661-sgMUC4-E3(F+E) (Addgene # 51025) were a gift from Bo Huang and Stanley Qi (1).

To eliminate the red fluorescence from sgRNA plasmids, *mCherry* gene was truncated from pSLQ1651-sgTelomere(F+E) and pSLQ1661-sgMUC4-E3(F+E) plasmids by digestion with AgeI + SgrAI and ligation of compatible ends.

pSLQ1661-sgMUC1-E1(F+E) with truncated *mCherry* was generated by Gibson assembly using pSLQ1661-sgMUC4-E3(F+E) with truncated *mCherry* and replacing sgMUC4-E3 with sgMUC1-E1 sequence with the use of the following primers:

Forward Fragment A: CCGCGCCACATAGCAGAACT TTAAA
Reverse Fragment A: tgggctgggggggcggtggagcCAACAA GGTGGTTCTCCAAGGGA
Forward Fragment B: gctccaccgccccccagcccaGTTTAA GAGCTATGCTGGAAACA
Reverse Fragment B: TTTAAAGTTCTGCTATGTGG CGCGG
The underlined sequence corresponds to sgMUC1-E1 sequence (1).

Polycistronic vectors were generated by gene synthesis and cloned into a pUC57 backbone by GenScript.

Sequences are listed below:

>hU6 Promoter_Plant $tRNA^{Gly}$_sgRNA MUC1-E1(F+E)_ Plant $tRNA^{Gly}$_sgRNA MUC4-E3(F+E)_Terminator:

TTTCCCATGATTCCTTCATATTTGCATATACG
ATACAAGGCTGTTAGAGAGATAATTGGAATTA
ATTTGACTGTAAACACAAAGATATTAGTACAA
AATACGTGACGTAGAAAGTAATAATTTCTTGG
GTAGTTTGCAGTTTTAAAATTATGTTTTAAAATG
GACTATCATATGCTTACCGTAACTTGAAAGTATT
TCGATTTCTTGGCTTTATATATCTTGTGGAAAGG
ACGAACAAAGCACCAGTGGTCTAGTGGTAGAA
TAGTACCCTGCCACGGTACAGACCCGGGTTCG
ATTCCCGGCTGGTGCAGCTCCACCGCCCCCCC
AGCCCAGTTTAAGAGCTATGCTGGAAACAGCA
TAGCAAGTTTAAATAAGGCTAGTCCGTTATCA
ACTTGAAAAAGTGGCACCGAGTCGGTGCAACA
AAGCACCAGTGGTCTAGTGGTAGAATAGTACC
CTGCCACGGTACAGACCCGGGTTCGATTCCCG
GCTGGTGCAGTGGCGTGACCTGTGGATGCTGG
TTTAAGAGCTATGCTGGAAACAGCATAGCAAG
TTTAAATAAGGCTAGTCCGTTATCAACTTGAAAA
AGTGGCACCGAGTCGGTGCTTTTTTGTTT

>hU6 Promoter_Human $tRNA^{Gly}$_sgRNA MUC1-E1(F+E)_ Human $tRNA^{Gly}$_sgRNA MUC4-E3(F+E)_Terminator:

TTTCCCATGATTCCTTCATATTTGCATATACG
ATACAAGGCTGTTAGAGAGATAATTGGAATTA
ATTTGACTGTAAACACAAAGATATTAGTACAA
AATACGTGACGTAGAAAGTAATAATTTCTTGG
GTAGTTTGCAGTTTTAAAATTATGTTTTAAAATG
GACTATCATATGCTTACCGTAACTTGAAAGTATT
TCGATTTCTTGGCTTTATATATCTTGTGGAAAGG
ACGAACAAAGCATTGGTGGTTCAGTGGTAGAA
TTCTCGCCTGCCACGCGGGAGGCCCGGGTTCG
ATTCCCGGCCAATGCAGCTCCACCGCCCCCCC
AGCCCAGTTTAAGAGCTATGCTGGAAACAGCA
TAGCAAGTTTAAATAAGGCTAGTCCGTTATCA
ACTTGAAAAAGTGGCACCGAGTCGGTGCAACA
AAGCATTGGTGGTTCAGTGGTAGAATTCTCGC
CTGCCACGCGGGAGGCCCGGGTTCGATTCCCG
GCCAATGCAGTGGCGTGACCTGTGGATGCTGG
TTTAAGAGCTATGCTGGAAACAGCATAGCAAG
TTTAAATAAGGCTAGTCCGTTATCAACTTGAAAA
AGTGGCACCGAGTCGGTGCTTTTTTGTTT

Cell culture and transgene expression

HeLa, HeLa 1.3 (kindly provided by Titia De Lange, The Rockefeller University, USA), C2C12 (kindly provided by Pura Muñoz-Canoves, UPF Barcelona, Spain) and HEK293T cells were cultured in Dulbecco's modified Eagle's medium (DMEM) (#41965062, Gibco) supplemented with 10% Fetal Bovine Serum (FBS) (#10270106, Gibco), 1× penicillin/streptomycin (#15140122, Gibco). mES cells were cultured on gelatin (#ES-006-B, Merck) coated dishes in sLif medium composed by DMEM supplemented with 15% FBS, 1× penicillin/streptomycin, 1× GlutaMax (#35050061, Gibco), 1× sodium pyruvate (#11360070, Gibco), 1× MEM non-essential amino acid (#11140050, Gibco), 0.2% 2-Mercaptoethanol (#31350010, Gibco) and 1000 U/ml LIF ESGRO (#ESG1107, Merck). Transfections were performed in suspension with Fugene HD (#E2311, Promega) for HeLa, HEK293T and C2C12 and with Mouse ES Cell Nucleofector® Kit (#VAPH-1001, Lonza) for mESC under manufacturer's conditions and with equimolar amounts of plasmids. Transfected cells were directly plated on 8-well Lab-Tek I borosilicate chambers (#155411, Nunc) at a density of 3.5×10^5 cells/cm^2.

Live cell imaging and analysis

Transfected cells were imaged at 48 h post-transfection in DMEM without Phenol red (#21063029, Gibco) supplemented with 10% FBS, 1× penicillin/streptomycin. Images were acquired in a Leica TCS SP5 II confocal microscope, with a 63.0 × 1.4 NA HCX PL APO lambda blue oil immersion objective. To quantify the labeling efficiency and the intensity of loci, the complete nuclear volume of living

cells was imaged in 0.1 μm z-steps stacks at 700 Hz of bidirectional scanning and 95.55 μm pinhole. Images were analyzed in ImageJ. Maximum intensity Z projections of the entire volume imaged were generated for each file. For Signal to Noise Ratio (SNR) analysis, telomeres and *MUC4* loci were manually segmented using a circle with a diameter of 3 pixels to quantify the average intensity within loci. Five circles of the same dimension were randomly placed in regions that contain background to obtain the average background intensity and the noise (standard deviation of the background). SNR was calculated by dividing the signal (locus intensity—average background intensity) by the noise. Signal over background was measured to compare polycistronic vectors by generating a plot of intensity values across a 2 μm line along every locus. Every intensity curve was background corrected and normalized curves were averaged to obtain signal over background curves for each condition. The area under the curves was calculated by the trapezoidal method and normalized by h_tRNA.

For dynamic studies, living cells were imaged at 1400 Hz of bidirectional scanning speed, 191.1 μm of pinhole for 2000 frames at 5 or 10 Hz of frame rate. See Telomere tracking section for detailed analysis information.

Chromatin immunoprecipitation (ChIP)

Chromatin was prepared from HeLa cells 48h post-transfection as previously described (12). Chromatin immunoprecipitation (ChIP) was performed as previously published (12) with the following modifications. A total of 25 μg of chromatin were incubated with 50 μl Protein G dynabeads (#10003D, ThermoFisher) previously bound for 5 h at 4°C to 2 μl of rabbit anti-Cas9 (#C15310258–20, Diagenode) or 2 μl of whole molecule rabbit IgG as negative control (#ab37415, Abcam). qPCR was performed with Lightcycler 480 SYBR green I master (#4887352001, Roche) and the primers listed below using a Lightcycler 480 (Roche) qPCR instrument.

MUC1 sgRNA targeted region A Fw: AGGCTCTGCATC AGGCTCAG
MUC1 sgRNA targeted region A Rv: TCTTGGTGCTAT GGCTGGCA
MUC1 sgRNA targeted region B Fw: AGCCCACGGTGT CACCTC
MUC1 sgRNA targeted region B Rv: CGGGGCCGGCCT GGTGT
MUC4 sgRNA targeted region Fw: GCCACCCCTCTT CCTGTCAC
MUC4 sgRNA targeted region Rv: GTGACCTGTGGA TGCTGAGG
Untargeted region MUC4 A (Negative control) Fw: TCCA CACAGAGCAGGCACTC
Untargeted region MUC4 A (Negative control) Rv: CACT GCAAGGGGTCCAGGAA
Untargeted region MUC4 B (Negative control) Fw: TCAA TGGTGGTCGTGTGATT (1)
Untargeted region MUC4 B (Negative control) Rv: AAGT CGGTGCAGCTGTCTCT (1)

Immunolabeling for STORM

For STORM imaging, transfected cells (48 h post-transfection) were incubated in DMEM with NileRed 240 nm beads (#FP-0256–2, Spherotech) at 1:450 dilution for 30 min in the incubator. After washing three times for 5 min with growth medium, cells were further kept in the incubator with growth medium for another one hour. Cells were then washed once with phosphate-buffered saline (PBS) and fixed with 10% PFA (#43368, Alfa Aesar) 10 min at room temperature (RT) and then washed three times in PBS for 5 min each. For immunolabeling with anti-GFP nanobodies, cells were permeabilized with PBS—0.3% Triton X100 for 15 min at RT. Blocking was performed in PBS—4% Horse Serum (#26050088, Gibco)—1% bovine serum albumin (#A7906, Sigma) for 45 min at RT. AlexaFluor-647 labeled anti-GFP nanobodies (NHS conjugated) (13) were incubated in blocking buffer at 1:100 dilution for 30 min at RT in the dark. Cells were washed three times in PBS for 5 min each at RT. AF-647 anti-GFP nanobodies were a kind gift from Jonas Ries (EMBL Heidelberg, Germany).

STORM imaging and data analysis

STORM images were acquired in a N-STORM 4.0 microscope (Nikon) equipped with a CFI HP Apochromat TIRF 100 × 1.49 oil objective and a iXon Ultra 897 camera (Andor). Cells stained with anti-GFP nanobodies were imaged for 60 000 frames at 16 ms frame rate using continuous 405 nm illumination, which was gradually increased over the imaging duration. Conventional fluorescence images were taken at the beginning of each imaging cycle. Imaging buffer composition was 150 mM Tris–HCl pH 8.8—100 mM Cysteamine MEA (#30070, Sigma-Aldrich)—1% Glox Solution (0.5 mg/ml glucose oxidase, 40 mg/ml catalase (#G2133 and #C100, Sigma-Aldrich))—5% Glucose (#G8270, Sigma-Aldrich).

STORM images were analyzed and rendered in Insight3 as previously described (14,15). Localizations were identified based on an intensity threshold (minimum intensity 2000) and fit to a simple Gaussian with a width between 200 and 400 nm to determine the x and y positions. Images were rendered with localizations represented as uniform Gaussian peaks having a width of 9 nm. Same contrast parameters were applied to each image to allow one to one comparison and to allow proper visualization of both the background and foreground signals reflecting the overall signal density of the image. Identified loci were verified by overlapping super resolution images with conventional fluorescence images of GFP and AF647 where telomeres are enriched for GFP and AF647 signals. Individual loci were manually selected to quantify in Insight3 the number of localizations per telomere, and the elipticity of telomeres from σ_x and σ_y. Voronoi tessellation (16,17) was performed with a customized Matlab code based on ClusterViSu (16). A common threshold (maximum area of Voronoi polygon of 99.84 nm^2) was applied to all nuclei analyzed and an additional threshold for minimum number of localizations per cluster was adjusted considering the variability of background signal and labeling density observed between experiments, in order to obtain optimal telomere identification. Overlay of Voronoi tessellation to con-

ventional fluorescence images showed good correlation of the identified clusters with telomeres. The area of telomeres in nm^2 was calculated as the sum of Voronoi polygons that form a telomeric cluster. The density (number of localizations/μm^2) of telomeres was obtained with dividing the number of localizations of the telomeric cluster by its area. The density of the background was obtained by sampling three 1 μm^2 areas within every nucleus analyzed.

Telomere tracking

Videos were analyzed with a custom written Matlab-based software that combines TrackRecord (18) and @msdanalyzer (19) with custom algorithms. Loci with intensity values above a threshold of 30 (8-bit images) and dimensions within 5 × 5 pixels (subROI) were automatically identified by TrackRecord at every frame and then a 2D Gaussian fitting was performed to calculate the x and y coordinates of the loci. Tracks were generated using a nearest-neighbors approach. If a merging or splitting event occurred, the track was discarded. Further computational analysis was carried out to estimate the diffusion coefficient (D $\mu m^2/s$) of telomeres, the SNR and the duration of the tracks. The Time Mean Squared Displacement curves (T-MSD) were used for a linear fitting, using the first four points of each MSD curve corresponding to each individual track (20). Only those tracks longer than 10 frames were analyzed. Diffusion coefficients were obtained for every locus, data were plotted as a histogram of the logarithm of the diffusion coefficients of all the tracks and the diffusion coefficient of the whole population were reported as the mean of all the coefficients ± the standard deviation. Using the Time-Ensemble Mean Squared Displacement curve (TE-MSD), the global behaviour of the particles was studied. In all the cases, a confined type of motion was observed and the radius of confinement that represents the whole population of tracks was obtained. This radius was estimated as the square root of the MSD value of the horizontal asymptote and the error was calculated from the weighted standard deviation of the TE-MSD (21). The photobleaching kinetics were estimated by fitting the evolution of the number of counts per frame with a two-component exponential decay: N(t) = f1*exp(-kb1*t) + (1-f1)*exp(-kb2*t) (22).

Statistical analysis

Statistical analysis has been performed in Graphpad Prism (v5.04) and in Matlab 2014b. Unpaired two-tailed t test has been applied for statistical comparison of two experimental conditions. One way Anova with Tukey's multiple comparison test has been applied for statistical comparison of datasets with more than two conditions. Statistical significance is represented in the following manner: ns $P > 0.05$, *$P \leq 0.05$, **$P \leq 0.01$, ***$P \leq 0.001$, ****$P \leq 0.0001$.

RESULTS AND DISCUSSION

(Po)STAC improves labeling efficiency and signal to background ratio for genome visualization

We tested the effectiveness of **STAC** by labeling high-repeat sequences in telomeres (Figure 1A) as well as moderate-to-low repeat sequences in the *Mucin 1* and *4* (*MUC1* and *4*) loci (Figure 1D and Supplementary Figure S1A). Cells were transfected with equal total amount of dCas9-**STAC** and dCas9-GFP. SunTag containing 24 repeats of the peptide array (24X-**STAC**) improved labeling efficiency by 2.5-fold (Percentage of cells with detectable loci = 35, 69 and 87% for dCas9 alone, 10× **STAC** and 24× **STAC**, respectively; $n \geq 4$ experiments) (Figure 1B) and the SNR by 5.4-fold in the case of telomeres compared to dCas9-GFP (SNR calculated as the signal divided by the standard deviation of the background = 7.2 ± 3.7 SD, averaged over 248 telomeres, 26.7 ± 12.9 SD averaged over 620 telomeres and 38.6 ± 8.92 SD averaged over 638 telomeres for dCas9 alone, 10× **STAC** and 24× **STAC**, respectively; $n = 3$ experiments) (Figure 1C). The fluorescent puncta corresponding to the gene loci were only detected in cells expressing the sgRNA and no fluorescent puncta were detectable in control cells lacking sgRNA (Supplementary Figure S1A). The labeling of the *Mucin* loci was further validated using ChIP followed by qPCR (ChIP-qPCR) using an antibody against dCas9. dCas9 was enriched in regions of *MUC1* and *MUC4* genes containing the sgRNA target sequences and this enrichment was not observed for non-target regions (Supplementary Figure S2). Importantly, **STAC** was applicable to label genes in several cell lines including HeLa cells, HEK 293T cells, C2C12 cells and mouse embryonic stem cells (Supplementary Figure S3A).

In order to extend this labeling approach to multiple genes, we further designed a mammalian cell optimized polycistronic vector including a human $tRNA^{Gly}$ (h_tRNA vector) interspersed between the sgRNAs to enable expression of multiple sgRNAs using a single plasmid (**PoSTAC**, Supplementary Figure S1B). **PoSTAC** further allowed the expression of multiple genes, in this case *MUC1* and *MUC4,* simultaneously in single cells (Figure 1D) with an efficiency similar to single gene labeling and higher than co-transfection with plasmids containing individual sgRNAs (Figure 1E). ChIP-qPCR experiments confirmed that the detected loci indeed corresponded to *MUC1* and *MUC4* (Supplementary Figure S2). Labeling efficiency was higher when using the polycistronic vector optimized for human (h_tRNA) compared to p_tRNA (82.5 versus 65.9% cells with fluorescently detectable loci with h_ and p_tRNA, respectively, $n \geq 4$ experiments) (Figure 1E). Further, the fluorescence intensity of each locus was similar to single gene labeling with h_tRNA (AUC = 1 a.u. for single gene labeling averaged over 217 MUC4 loci versus 0.98 a.u. for multigene labeling averaged over 413 *MUC1/4* loci; $n = 3$ experiments), while slightly reduced for the p_tRNA vector (0.76 a.u. averaged over 322 *MUC1/4* loci; $n = 3$ experiments). HeLa cells are triploid for both *MUC1* and *MUC4*, therefore, we expected to visualize up to 6 or 12 loci depending on if the cells were in G1 or G2/S cell cycle phase, respectively. The number of loci indeed ranged from 1 to 12 with an average of 5.5 ± 0.69 SD and 4.4 ± 0.91 SD detected loci per cell for the h_tRNA and p_tRNA vectors, respectively (Figure 1F and Supplementary Figure S1C). In the case of h_tRNA vector, this number is close to the expected value of 6 since the large majority of cells were imaged in G1 having three copies of each gene. Cells containing less than six loci are likely either due to occasional not efficient

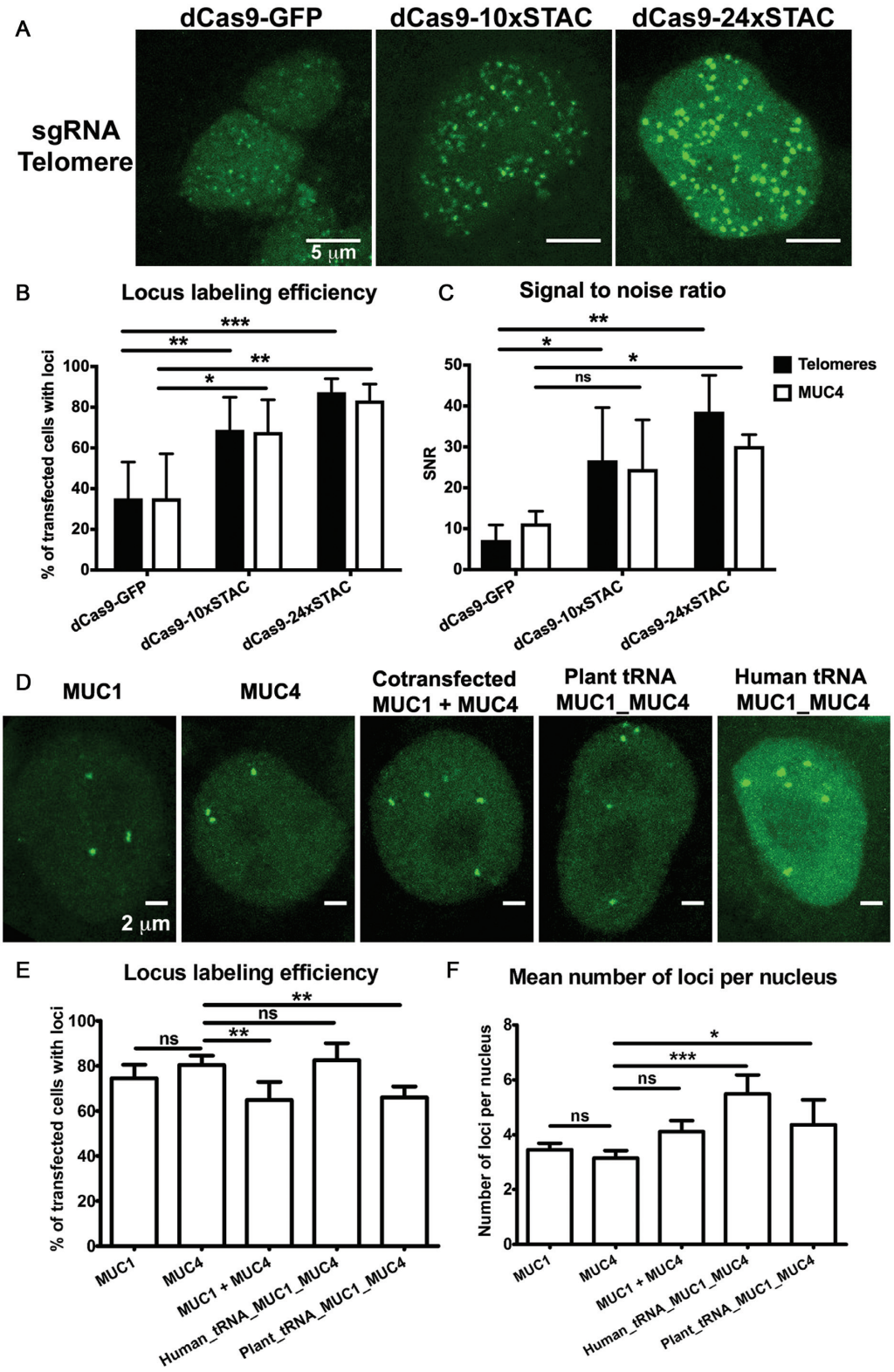

Figure 1. (**A**) Maximum intensity projections of confocal images of HeLa cells transfected with sgRNA *Telomere* and dCas9-GFP, dCas9–10x**STAC** or dCas9–24x**STAC**. (**B**) Labeling efficiency as percentage of transfected HeLa cells with detectable loci. $n \geq 4$ experiments. (**C**) SNR of telomeres and *MUC4* loci measured in HeLa cells transfected with dCas9-GFP, dCas9–10x**STAC** or dCas9–24x**STAC.** $n = 3$ experiments. (**D**) Maximum intensity projections of confocal images of HeLa cells transfected with dCas9–24x**STAC** and sgRNAs for *MUC1*, *MUC4*, *MUC1+MUC4*, *plant_tRNA_MUC1_MUC4* or *human_tRNA_MUC1_MUC4*. (**E**) Labeling efficiency as percentage of transfected HeLa cells with detectable loci. $n = 3$ experiments. (**F**) Mean number of loci detected per nucleus. $n = 3$ experiments. For all plots Mean ± SD is displayed. Stars indicate *P*-values (ns $P > 0.05$, $^{*}P \leq 0.05$, $^{**}P \leq 0.01$, $^{***}P \leq 0.001$) for one way Anova with Tukey's multiple comparison test.

cleavage of the tRNA or to HeLa cells containing less than three copies of one or both of the genes. Importantly, the average number of loci detected per cell was higher with the polycistronic vectors than the co-transfection strategy with single sgRNAs, further indicating the superior performance of this imaging strategy (Figure 1E and Supplementary Figure S1C).

STAC enables super-resolution imaging of telomere compaction in fixed cells

Telomere length is tightly regulated in mammalian cells and is key for cell survival. During normal cell homeostasis telomere length is rigorously controlled during DNA replication (23). Short telomeres induce cellular senescence, apoptosis (23) and age-associated diseases (24). Telomere length is maintained in cancer cells, which can elongate telomeres to escape senescence and proliferate indefinitely (23). Adult stem cells have long telomeres, which are also elongated during somatic cell reprogramming (25). The mechanisms by which telomeres protect chromosome ends from double-stranded break repair and solve the end protection problem is subject to intense debate (26–28). Recent super-resolution studies of telomere compaction have relied on either harsh sample preparation methods such as DNA fluorescence *in situ* hybridization (FISH) (26–28) or indirect visualization of telomere-binding proteins (26) to study telomere compaction at high resolution. Importantly, these methods are not compatible with visualizing genome dynamics in living cells. For these reasons an imaging method to visualize dynamics and compaction of genomic regions like telomeres with high spatiotemporal resolution is highly valuable for many biological applications. However, the poor labeling efficiency as well as the low signal-to-background ratio of the CRISPR-dCas9 label has made its application to super-resolution studies highly challenging.

We therefore applied **STAC** to image telomeres at high resolution in fixed cells in two different HeLa cell lines that have different telomere lengths (HeLa and HeLa 1.3 with average telomere lengths of 6 and 23 kb, respectively) (29). The labeling efficiency was similar between HeLa (83.4% of cells with detectable telomeres) and HeLa 1.3 cells (87.9% of cells with detectable telomeres) and telomeres appeared brighter in the HeLa 1.3 cells as expected from their longer lengths (Supplementary Figure S3B and C). We next analyzed the telomeres in the two cell lines using stochastic optical reconstruction microscopy (STORM) by labeling the dCas9-STAC/scFv-GFP complex with an AlexaFluor647-tagged anti-GFP nanobody (13) (Figure 2A). We observed that telomere loci overlapped with those detected in the conventional fluorescence images but whose size was much smaller (Figure 2A). The detected localization density was much higher in the telomere loci than background regions not containing the specific loci (27393 ± 2875 SD and 399.3 ± 166.4 SD localizations per μm^2 in telomere loci versus background, respectively). On average, 3.7-fold higher fluorophore localizations were detected from the longer telomeres in HeLa 1.3 cells (Average number of Localizations = 320 ± 326.7 SD per telomere for HeLa and 1179 ± 931.3 SD per telomere for HeLa 1.3 cells; $n = 3$ experiments and $n =$ 46 and 44 cells, HeLa and HeLa 1.3, respectively) (Figure 2B). This increase in the number of detected localizations per telomere correlates well with the previously determined 3.8-fold increase in the number of repeats for telomeres in HeLa 1.3 cells (29). Telomeres were slightly elliptical in their shape with a minor-to-major axis ratio of 0.82 ± 0.1 SD and 0.85 ± 0.1 SD for HeLa and HeLa 1.3 cells, respectively. We used Voronoi tessellation (16,17) to segment the telomeres in the super-resolution images (Figure 2C and D) and determined their area by summing over the area of individual Voronoi cells for each telomere (Figure 2C and D). Telomere area was increased by 2.8-fold in HeLa1.3 cells (Figure 2C) corresponding to a volume increase of roughly 4.7 fold. The increase in volume was only slightly larger than the increase observed for the number of localizations per telomere and the linear length of the telomeres. These results therefore suggest that telomere compaction is not very different in the two cell lines. Super-resolution imaging was possible not only for high-repeat sequences such as telomeres but also for moderate-to-low repeat sequences such as *MUC4*, allowing visualization and discrimination of nearby alleles too close to be properly resolved by conventional microscopy (Supplementary Figure S4).

STAC enables live-cell imaging of telomere dynamics

Live cell compatibility of the **STAC** labeling approach further enabled visualization of telomere dynamics at high temporal resolution. Tracking of individual telomeres in HeLa cells (Supplementary Videos S1–2 and Figure 3A) showed that telomere dynamics were unaffected by the increased GFP-recruitment to the gene locus with STAC since the diffusion coefficient of telomeres labeled with STAC were comparable to dCas9-GFP alone tagging strategy (Figure 3B). Both populations showed comparable confined movement (Diffusion coefficient of $10.4*10^{-4}$ $\mu m^2/s$ ± $6.1*10^{-4}$ SD and $9.92*10^{-4}$ $\mu m^2/s$ ± $5.51*10^{-4}$ SD; $P =$ 0.03. Radius of Confinement of 123 nm ± 43 SD and 109 nm ± 38 SD for dCas9 and 24× STAC, respectively). However, compared to dCas9-GFP alone, telomeres labeled with **STAC** showed reduced photobleaching over time (Supplementary Videos S1–2 and Figure 3C) and more telomeres could be tracked per cell with **STAC** (Figure 3D). Therefore, **STAC** enables following genome dynamics for longer time. In addition, typically signal intensity is a limitation for fast image acquisition, and hence STAC enables faster acquisition speeds by enhancing the SNR. However, caution must be taken as for any other live-cell imaging method to minimize phototoxicity, which is often a limiting factor in every live-cell imaging experiment. Finally, telomeres in HeLa 1.3 cells had lower diffusion coefficient (Diffusion coefficient of $4.32*10^{-3}$ $\mu m^2/s$ ± $4*10^{-3}$ SD and $7.23*10^{-3}$ $\mu m^2/s$ ± $5*10^{-3}$ SD, for HeLa 1.3 and HeLa, respectively; $P = 9.8e\text{-}41$) and lower radius of confinement (Radius of confinement 142 nm ± 40 SD and 181 nm ± 50 SD for HeLa 1.3 and HeLa, respectively) compared to HeLa cells, likely due to the increased volume they occupy in physical space (Figure 3E and F). These results further demonstrate the power of **STAC** as it can be readily used for correlative studies of gene dynamics in living cells and super-resolution imaging of the architecture of these genes in fixed cells.

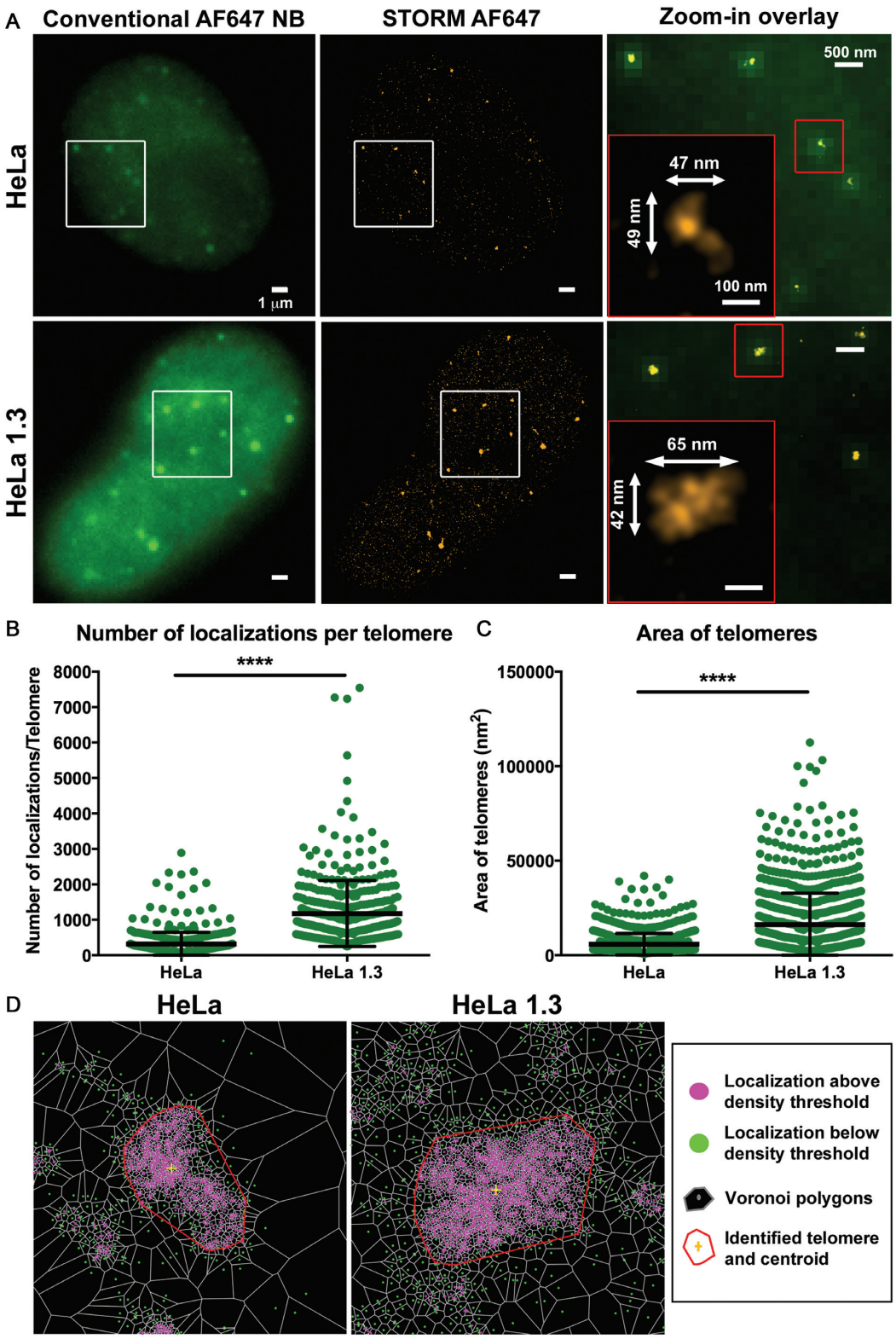

Figure 2. (**A**) Super resolution images (STORM) of fixed HeLa (top) and HeLa 1.3 (bottom) cells transfected with dCas9–24x**STAC** and sgRNA *Telomere*, immunolabeled with AlexaFluor647 anti-GFP nanobody (NB). From left to right: conventional AF647 fluorescence image (green), STORM image (orange), zoom-in overlay of conventional and STORM image (white square) and high magnification zoom-in (red square). The numbers represent the standard deviation of the localizations along the *x*- and *y*-axis. (**B**) Number of localizations of telomeres in HeLa and HeLa 1.3 cells. $n = 3$ experiments, $n =$ 46 (HeLa) and 44 (HeLa 1.3) cells. (**C**) Area of telomeres identified by Voronoi tesselation analysis expressed in nm^2. (**D**) Example of Voronoi tessellation in HeLa and HeLa 1.3, the telomeres shown correspond to the high magnification panels in (A). For all plots Mean ± SD is displayed. Stars indicate *P*-values (****$P \leq 0.0001$) for two-tailed unpaired *t*-test.

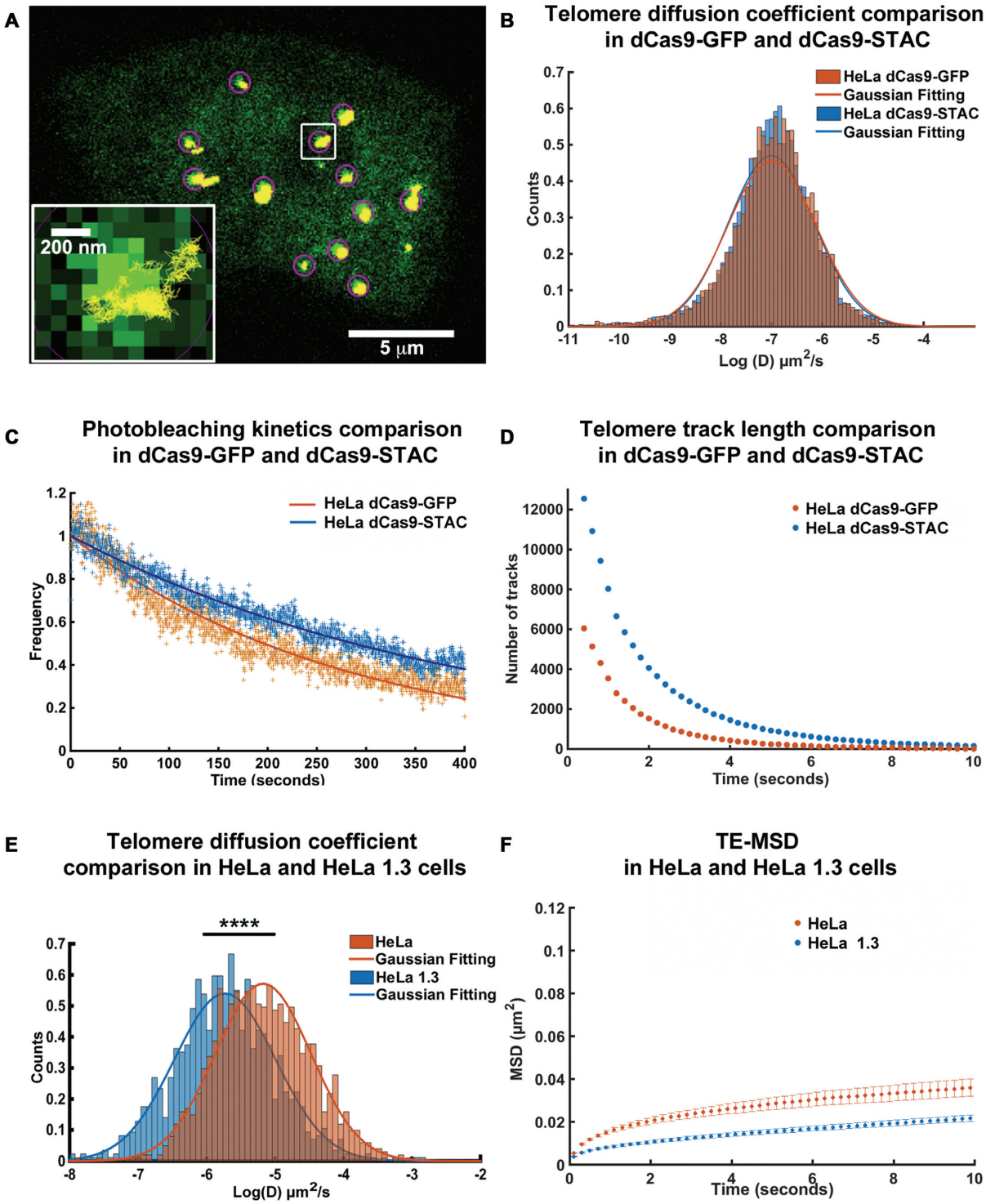

Figure 3. (**A**) Representative image showing telomere tracks over 2000 frames. (**B**) LogD (Logarithm of Diffusion coefficient) plot for HeLa telomere tracks imaged at 5 Hz with dCas9-GFP and dCas9–24x**STAC**. $n = 7103$ and 14450 tracks for dCas9-GFP and dCas9–24x**STAC**, respectively. (**C**) Photobleaching kinetics for HeLa telomere loci imaged at 5 Hz with dCas9-GFP and dCas9–24x**STAC** for the same cells and tracks of (B), $n = 7103$ and 14450 tracks for dCas9-GFP and dCas9–24x**STAC**, respectively. The plot shows the normalized number of localizations per frame (crosses) and the corresponding two-component exponential fit (lines). Photobleaching constants for HeLa dCas9-GFP $k2^{-1} = 282$ s and for HeLa dCas9–24x**STAC** $k2^{-1} = 415$ s. (**D**) Track length plots for telomere tracks imaged at 5 Hz with dCas9-GFP and dCas9–24x**STAC** in equal number of cells. $n = 6$ cells per condition with $n = 7103$ and 14450 tracks for dCas9-GFP and dCas9–24x**STAC**, respectively. (**E**) Diffusion coefficient comparison of HeLa and HeLa 1.3 telomere tracks imaged at 10 Hz. $n = 1260$ and 1068 tracks for HeLa and HeLa 1.3, respectively. Stars indicate P-values (****$P \leq 0.0001$) for two-tailed unpaired t-test. (**F**) Time Ensemble Mean Squared Displacement (TE-MSD) for HeLa and HeLa 1.3 telomere tracks imaged at 10 Hz. $n = 1260$ and 1068 tracks for HeLa and HeLa 1.3, respectively (same cells as panel E). Radius of confinement of $R = 142 \pm 40$ nm and $R = 181 \pm 50$ nm. The error bars were calculated as the weighted standard deviation of the MSD values divided by the square root of the number of degrees of freedom in the weighted mean.

CONCLUSION

Overall, we demonstrate increased labeling efficiency and enhanced signal in visualizing multiple genomic loci in both living and fixed cells by combining CRISPR/dCas9 with SunTag and polycistronic vectors. **STAC** and **PoSTAC** are enhanced labeling strategies that enabled both longer term and faster imaging of genome dynamics in living cells as well as super-resolution imaging of their spatial organization in fixed cells (Supplementary Figure S5). These advancements overcome limitations of previous methods such as DNA FISH in visualizing genomic sequences with high-spatiotemporal resolution. The use of polycistronic vectors is not limited to gene visualization but can also be used for activating/repressing multiple genes simultaneously with CRISPR-Cas9 and for multiple gene editing in mammalian cells. In addition, PoSTAC should enhance visualization of unique, non-repetitive sequences by enabling efficient delivery of multiple sgRNAs into single cells using minimal number of plasmids and by enhancing the signal over background via the use of SunTag. In the case of multi-gene labeling, the identity of different loci labeled by PoSTAC can potentially be determined by carrying out correlative live-cell imaging and DNA FISH after fixation, as recently demonstrated (30). In the future PoSTAC can potentially be used for multi-color imaging by encoding sgRNAs specifically recognized by different Cas9 orthologs such as *Streptococcus pyogenes* Sp dCas9, *Neisseria meningitidis* Nm dCas9 and *Streptococcus thermophilus* St1 dCas9 (2) or even Cpf1 orthologs.

DATA AVAILABILITY

Data is available upon request.

SUPPLEMENTARY DATA

Supplementary Data are available at NAR Online.

ACKNOWLEDGEMENTS

Authors acknowledge Prof. Titia De Lange (The Rockefeller University), Prof. Pura Muñoz-Cánoves (Pompeu Fabra University), Dr Jonas Ries (EMBL Heidelberg) and Dr Bo Huang (UCSF) for kindly sharing HeLa 1.3 cells, C2C12 cells, GFP nanobodies and Insight3, respectively. Authors acknowledge Dr Jason Otterstrom for his help with Voronoi tessellation analysis.

FUNDING

European Union's Horizon 2020 Research and Innovation Programme [CellViewer No 686637 to M.L., M.P.C.]; Ministerio de Economia y Competitividad [BFU2013–49867-EXP to M.L., M.P.C.]; Fundació Cellex Barcelona (to M.L); European Union Seventh Framework Programme under the European Research Council Grants [337191-MOTORS to M.L.]; 'Severo Ochoa' Programme for Centres of Excellence in R&D [SEV-2015- 0522 to M.L.]; Ministerio de Economia y Competitividad and FEDER Funds [BFU2014–54717-P, BFU2015–71984-ERC to M.P.C.]; AGAUR Grant [2014 SGR1137 to M.P.C.]; Spanish Ministry of Economy and Competitiveness (to M.P.C.); Centro de Excelencia Severo Ochoa [2013–2017 to M.P.C.]; CERCA Programme/Generalitat de Catalunya (to M.P.C); Ministerio de Ciencia e Innovacion FPI (to F.A.); People Program (Marie Curie Actions) FP7/2007–2013 under REA grant [608959 to M.V.N.]. Funding for open access charge: European Union's Horizon 2020 Research and Innovation Programme [CellViewer No 686637].
Conflict of interest statement. None declared.

REFERENCES

1. Chen,B., Gilbert,L.A., Cimini,B.A., Schnitzbauer,J., Zhang,W., Li,G.W., Park,J., Blackburn,E.H., Weissman,J.S., Qi,L.S. *et al.* (2013) Dynamic imaging of genomic loci in living human cells by an optimized CRISPR/Cas system. *Cell*, **155**, 1479–1491.
2. Ma,H., Naseri,A., Reyes-Gutierrez,P., Wolfe,S.A., Zhang,S. and Pederson,T. (2015) Multicolor CRISPR labeling of chromosomal loci in human cells. *Proc. Natl. Acad. Sci. U.S.A.*, **112**, 3002–3007.
3. Shechner,D.M., Hacisuleyman,E., Younger,S.T. and Rinn,J.L. (2015) Multiplexable, locus-specific targeting of long RNAs with CRISPR-Display. *Nat. Methods*, **12**, 664–670.
4. Shao,S., Zhang,W., Hu,H., Xue,B., Qin,J., Sun,C., Sun,Y., Wei,W. and Sun,Y. (2016) Long-term dual-color tracking of genomic loci by modified sgRNAs of the CRISPR/Cas9 system. *Nucleic Acids Res.*, **44**, e86.
5. Qin,P., Parlak,M., Kuscu,C., Bandaria,J., Mir,M., Szlachta,K., Singh,R., Darzacq,X., Yildiz,A. and Adli,M. (2017) Live cell imaging of low- and non-repetitive chromosome loci using CRISPR-Cas9. *Nat. Commun.*, **8**, 14725.
6. Chen,B., Guan,J. and Huang,B. (2016) Imaging specific genomic DNA in living cells. *Annu. Rev. Biophys.*, **45**, 1–23.
7. Tanenbaum,M.E., Gilbert,L.A., Qi,L.S., Weissman,J.S. and Vale,R.D. (2014) A protein-tagging system for signal amplification in gene expression and fluorescence imaging. *Cell*, **159**, 635–646.
8. Schiffer,S., Rosch,S. and Marchfelder,A. (2002) Assigning a function to a conserved group of proteins: the tRNA 3′-processing enzymes. *EMBO J.*, **21**, 2769–2777.
9. Evans,D., Marquez,S.M. and Pace,N.R. (2006) RNase P: interface of the RNA and protein worlds. *Trends Biochem. Sci.*, **31**, 333–341.
10. Xie,K., Minkenberg,B. and Yang,Y. (2015) Boosting CRISPR/Cas9 multiplex editing capability with the endogenous tRNA-processing system. *Proc. Natl. Acad. Sci. U.S.A.*, **112**, 3570–3575.
11. Port,F. and Bullock,S.L. (2016) Augmenting CRISPR applications in Drosophila with tRNA-flanked sgRNAs. *Nat. Methods*, **13**, 852–854.
12. Neguembor,M.V., Xynos,A., Onorati,M.C., Caccia,R., Bortolanza,S., Godio,C., Pistoni,M., Corona,D.F., Schotta,G. and Gabellini,D. (2013) FSHD muscular dystrophy region gene 1 binds Suv4-20h1 histone methyltransferase and impairs myogenesis. *J. Mol. Cell Biol.*, **5**, 294–307.
13. Ries,J., Kaplan,C., Platonova,E., Eghlidi,H. and Ewers,H. (2012) A simple, versatile method for GFP-based super-resolution microscopy via nanobodies. *Nat. Methods*, **9**, 582–584.
14. Rust,M.J., Bates,M. and Zhuang,X. (2006) Sub-diffraction-limit imaging by stochastic optical reconstruction microscopy (STORM). *Nat. Methods*, **3**, 793–795.
15. Bates,M., Huang,B., Dempsey,G.T. and Zhuang,X. (2007) Multicolor super-resolution imaging with photo-switchable fluorescent probes. *Science*, **317**, 1749–1753.
16. Andronov,L., Orlov,I., Lutz,Y., Vonesch,J.L. and Klaholz,B.P. (2016) ClusterViSu, a method for clustering of protein complexes by Voronoi tessellation in super-resolution microscopy. *Sci. Rep.*, **6**, 24084.
17. Levet,F., Hosy,E., Kechkar,A., Butler,C., Beghin,A., Choquet,D. and Sibarita,J.B. (2015) SR-Tesseler: a method to segment and quantify localization-based super-resolution microscopy data. *Nat. Methods*, **12**, 1065–1071.
18. Mazza,D., Ganguly,S. and McNally,J.G. (2013) Monitoring dynamic binding of chromatin proteins in vivo by single-molecule tracking. *Methods Mol. Biol.*, **1042**, 117–137.
19. Tarantino,N., Tinevez,J.Y., Crowell,E.F., Boisson,B., Henriques,R., Mhlanga,M., Agou,F., Israel,A. and Laplantine,E. (2014) TNF and

IL-1 exhibit distinct ubiquitin requirements for inducing NEMO-IKK supramolecular structures. *J. Cell Biol.*, **204**, 231–245.
20. Michalet,X. and Berglund,A.J. (2012) Optimal diffusion coefficient estimation in single-particle tracking. *Phys. Rev. E Stat. Nonlin. Soft Matter Phys.*, **85**, 061916.
21. Kusumi,A., Sako,Y. and Yamamoto,M. (1993) Confined lateral diffusion of membrane receptors as studied by single particle tracking (nanovid microscopy). Effects of calcium-induced differentiation in cultured epithelial cells. *Biophys. J.*, **65**, 2021–2040.
22. Mazza,D., Abernathy,A., Golob,N., Morisaki,T. and McNally,J.G. (2012) A benchmark for chromatin binding measurements in live cells. *Nucleic Acids Res.*, **40**, e119.
23. Shay,J.W. (2016) Role of Telomeres and Telomerase in Aging and Cancer. *Cancer Discov.*, **6**, 584–593.
24. Stanley,S.E. and Armanios,M. (2015) The short and long telomere syndromes: paired paradigms for molecular medicine. *Curr. Opin. Genet. Dev.*, **33**, 1–9.
25. Marion,R.M., Strati,K., Li,H., Tejera,A., Schoeftner,S., Ortega,S., Serrano,M. and Blasco,M.A. (2009) Telomeres acquire embryonic stem cell characteristics in induced pluripotent stem cells. *Cell Stem Cell*, **4**, 141–154.
26. Bandaria,J.N., Qin,P., Berk,V., Chu,S. and Yildiz,A. (2016) Shelterin protects chromosome ends by compacting telomeric chromatin. *Cell*, **164**, 735–746.
27. Vancevska,A., Douglass,K.M., Pfeiffer,V., Manley,S. and Lingner,J. (2017) The telomeric DNA damage response occurs in the absence of chromatin decompaction. *Genes Dev.*, **31**, 567–577.
28. Timashev,L.A., Babcock,H., Zhuang,X. and de Lange,T. (2017) The DDR at telomeres lacking intact shelterin does not require substantial chromatin decompaction. *Genes Dev.*, **31**, 578–589.
29. Takai,K.K., Hooper,S., Blackwood,S., Gandhi,R. and de Lange,T. (2010) In vivo stoichiometry of shelterin components. *J. Biol. Chem.*, **285**, 1457–1467.
30. Guan,J., Liu,H., Shi,X., Feng,S. and Huang,B. (2017) Tracking multiple genomic elements using correlative CRISPR imaging and sequential DNA FISH. *Biophys. J.*, **112**, 1077–1084.